ARTICLE   OPEN

Collective magnetic Higgs excitation in a pyrochlore ruthenate

Dirk Wulferding [1,2,10], Junkyoung Kim[3,10], Mi Kyung Kim[1,2], Yang Yang[4], Jae Hyuck Lee [1,2], Dongjoon Song [1,2], Dongjin Oh [1,2], Heung-Sik Kim [5], Li Ern Chern[6], Yong Baek Kim[6], Minji Noh[1,2,7], Hyunyong Choi[2,7], Sungkyun Choi[8,9], Natalia B. Perkins[4], Changyoung Kim[1,2 ✉] and Seung Ryong Park[3 ✉]

The emergence of scalar Higgs-type amplitude modes in systems where symmetry is spontaneously broken has been a highly successful, paradigmatic description of phase transitions, with implications ranging from high-energy particle physics to low-energy condensed matter systems. Here, we uncover two successive high temperature phase transitions in the pyrochlore magnet $Nd_2Ru_2O_7$ at $T_N = 147$ K and $T^* = 97$ K, that lead to giant phonon instabilities and culminate in the emergence of a highly coherent excitation. This coherent excitation, distinct from other phonons and from conventional magnetic modes, stabilizes at a low energy of 3 meV. We assign it to a collective Higgs-type amplitude mode, that involves bond energy modulations of the Ru_4 tetrahedra. Its striking two-fold symmetry, incompatible with the underlying crystal structure, highlights the possibility of multiple entangled broken symmetries.

INTRODUCTION

The Higgs mechanism, first invoked to describe spontaneous symmetry breaking in superconductors, has since proven successful in describing masses of the W and Z bosons in the standard model[1], in describing collective excitations in superconducting condensates and superfluids[2], and in describing quantum magnets close to criticality[3,4]. In these scenarios, Higgs modes of scalar nature are a crucial component of spontaneous symmetry breaking. Very recently, axial Higgs modes have been discussed in the context of condensed matter physics, where the spontaneous and simultaneous breaking of different symmetries gives rise to the interplay of multiple order parameters[5]. As axial Higgs modes may be highly relevant for models describing physics beyond the standard model, e.g., dark matter[6,7], correlated electron systems with entangled degrees of freedom can serve as excellent playgrounds to explore exotic, non-scalar amplitude-Higgs modes and test proposed models[5].

Among correlated electron systems, $4d$ transition metal oxides (TMOs) provide exceptional platforms for exploring complex emergent phenomena due to their intricate interplay of spin and orbital degrees of freedom[8,9]. Examples include spin fractionalization into Majorana fermions due to bond-dependent exchange frustration in Kitaev honeycomb magnets[9–13], unconventional superconductivity[14], spin-ice states with emergent magnetic monopoles and unique quantum electrodynamics[15–18], and materials with topologically non-trivial electronic and magnon band structures[19–21], to name a few. Particularly, the family of $4d$ transition metal pyrochlore oxides exhibits a diverse array of exotic phenomena, driven by the interplay between geometrical frustration, electronic interactions, spin-orbit coupling, and lattice instabilities[22,23].

The diverse physical properties of these $4d$ TMO pyrochlores with the general chemical formula $A_2M_2O_7$ are determined by the choice of A-site ions and transition metal ions M. The Mott insulators $A_2Ru_2O_7$ with a series of rare-earth elements (A = Pr – Lu, Y), in which Ru^{4+} ions (electron configuration $4d^4$) are expected to carry $S = 1$ spins and angular moment $L = 1$ according to Hund's rule, are of special interest as candidate materials to study magnetic properties of frustrated spin-1 antiferromagnetism[24–27]. Particularly, a number of different spin structures both with and without topological magnons may be realized in this class of materials, depending on microscopic details[22]. Yet, the lack of high quality single crystals of the $A_2Ru_2O_7$ series has hindered a systematic experimental exploration of their exact ground states and emergent magnetic anisotropies so far. Additional complications arise from the fact that spin-orbit coupling is comparable to the super-exchange scale. Therefore, a magnetic condensation of Van Vleck excitons may occur[3,28], which will behave as the magnetic degrees of freedom and lead to either spin-nematic or amplitude fluctuations.

The compound of our interest, $Nd_2Ru_2O_7$, consists of Ru^{4+} ions octahedrally coordinated by O^{2-} ions to form larger Ru tetrahedra building blocks. Below $T_N = 147$ K, Ru magnetic moments order antiferromagnetically (see Supplementary Note 1, and Supplementary Figs. 1 and 2), although a dispute exists about the nature of the ordering – while some experiments point towards a long-range ordered state[29], an earlier neutron diffraction study on powder samples of $Nd_2Ru_2O_7$ suggested a spin-glass or short-range ordered state[30].

Here, we employ polarization-resolved Raman spectroscopy to study the symmetry and the temperature-dependence of magnetic and phonon excitations in high quality $Nd_2Ru_2O_7$ single crystals. Below the Néel temperature $T_N = 147$ K of the Ru ions we uncover an extended temperature regime of spin-lattice coupled fluctuations that result in a second phase transition $T^* = 97$ K and give rise to an anomalous, well-defined low-energy amplitude excitation. Our observations suggest that at intermediate temperatures $Nd_2Ru_2O_7$ is dominated by bond energy fluctuations
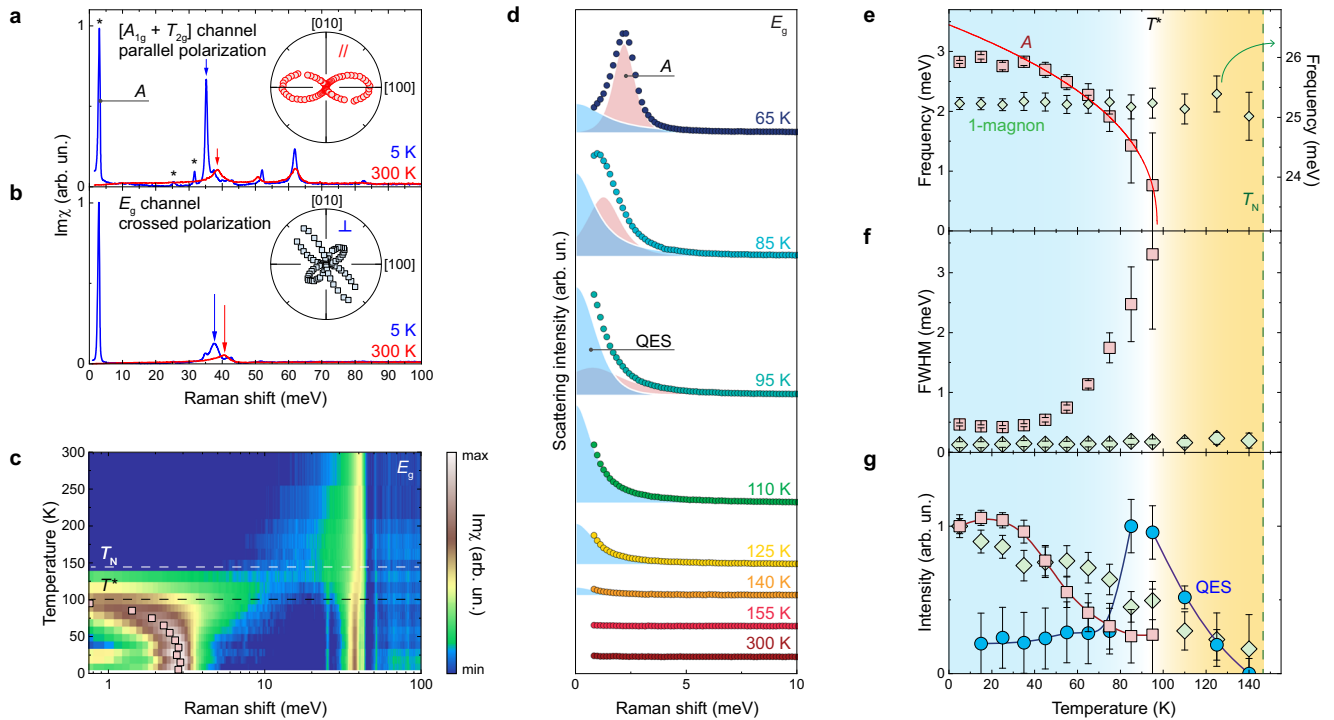
Fig. 1 Temperature dependence of magnetic modes. a, b Bose-corrected Raman intensity (Imχ) measured at 5 K (blue curve) and 300 K (red curve) in the $A_{1g}+T_{2g}$ ($e_{in} = e_{out} = [110]$) and the E_g ($e_{in} = [110]$, $e_{out} = [\bar{1}10]$) symmetry channels, respectively. Arrows mark the T_{2g} phonon **a** and the E_g phonon **b**. The insets plot the angular dependent intensity of excitation A at 5 K in parallel and crossed polarization. **c** Color contour plot of the temperature dependence in E_g symmetry. Note that the Raman shift is shown on a logarithmic scale to emphasize low lying excitations. Square symbols trace the evolution of excitation A. The dashed lines mark T_N and T^*. **d** Raman spectra measured in E_g symmetry at selected temperatures through T_N (full circles). The emergent quasi-elastic scattering (QES) and excitation A are shaded. **e–g** Temperature dependence of the energy, linewidth, and intensity of the low-energy excitation A (red squares) together with the one-magnon excitation at 25 meV (pale green diamonds). The solid red curve is a mean-field fit to the energy (see text for details). The blue circles in **g** show the intensity of quasi-elastic scattering. The dashed green line marks T_N. Error bars in **e–g** indicate ± 1 standard deviation around the mean value.

from which a collective excitation emerges, which is consistent with a Higgs-type nematic amplitude mode.

RESULTS

Magnetic excitations

Below 1.8 K, Nd^{3+} spins are found to order in an all-in-all-out state[31]. In our study we only focus on temperatures above 5 K, therefore we can consider the Nd spins to be paramagnetic[29] and thus assign all magnetic excitations in our study to Ru ions. In Fig. 1a, b we plot Bose-corrected Raman data obtained at 300 and 5 K in two different scattering geometries, distinguishing between the three allowed symmetry channels $A_{1g}+T_{2g}$ and E_g (see also Supplementary Note 2 and Supplementary Fig. 3). All spectral features in the energy range 33–90 meV can be assigned to phonon modes, which we will discuss in more detail below. Three low-energy excitations emerge below T_N at 32, 25, and 3 meV, marked by asterisks in Fig. 1a.

We can assign the two higher-lying excitations at 32 and 25 meV to one-magnon modes, based on their symmetry, their energies (see Supplementary Note 3 and Supplementary Fig. 4), and their temperature dependence discussed below. Based on our analysis of symmetry-allowed spin configurations on the $S = 1$ pyrochlore lattice, the best description of the 32 and 25 meV one-magnon modes in terms of energy and number of branches at $q = 0$ is achieved for the all-in-all-out ordered state of Ru magnetic moments. This result is somewhat at odds with previous powder neutron diffraction results[30], where a spin-glass state or XY spin structure was assigned to $Nd_2Ru_2O_7$. Our assignment is based on

experiments restricted to $q = 0$. Furthermore, additional terms added to the Hamiltonian, such as substantial spin-orbit coupling, may modify this scenario and other spin configurations may be better candidates to describe our experimental data. Eventually, a detailed temperature-dependent inelastic neutron scattering study on high-quality phase-pure single crystalline $Nd_2Ru_2O_7$ will help to settle this issue.

Phenomenologically similar one-magnon excitations have been reported in the spin-1/2 pyrochlore compound $Y_2Ir_2O_7$[32], as well as in recent Raman scattering experiments from powder samples of $A_2Ru_2O_7$ (A = Y, Sm, Eu, Ho, Er)[33]. In addition, the overall small intensities of these modes relative to other phonon modes can support our assignment, as magnetic Raman scattering processes are generally less intense than phononic Raman scattering processes.

In contrast to these one-magnon modes of weak scattering intensities, the peak at 3 meV (in the following referred to as the A-mode) dominates the Raman spectra at low temperatures. The angular dependence of its intensity, measured at $T = 5$ K, is plotted as a function of light polarization within the ab plane with parallel polarization (inset of Fig. 1a) and crossed polarization (inset of Fig. 1b). Its two-fold symmetry in the parallel polarization and the modulation of the lobe's amplitudes in the cross polarization are incompatible with expected A_1, T_2, or E irreducible representations of the T_d lattice point group of the pyrochlore lattice, and require a Raman tensor with antisymmetric tensor elements. Therefore these results are also different from the four-fold symmetries expected and observed for conventional (i.e., one-magnon or two-magnon) magnetic modes (see Supplementary Notes 4, 5, and Supplementary Fig. 5 for a detailed symmetry analysis).

To better understand the nature of this unconventional excitation, we now turn to an analysis of its thermal evolution. The temperature dependent Raman data is shown in a color contour plot in Fig. 1c (see Supplementary Note 6 and Supplementary Fig. 6 for details on the fitting procedure). As we approach T_N from the high temperature side, there is a continuous increase in a broadened spectral weight at the left shoulder of the E_g phonon around 40 meV (see the green-colored background between 10 and 40 meV). In agreement with previous Raman studies on pyrochlore magnets[34], we assign this continuum to paramagnetic fluctuations. Once T_N is reached and crossed, this spectral weight is transferred towards zero energies, forming an increasing quasi-elastic scattering signal. Note that the spectral weight is not necessarily a conserved quantity through the transition process. Nonetheless, the transfer of spectral weight suggests an intimate link between the two signals. The quasi-elastic signal can be well fitted by a single Lorentzian line-shape centered at $E = 0$, as demonstrated in Fig. 1d for the temperatures 110–140 K. Such behavior is characteristic for a phase transition and originates from increasing zero-energy density fluctuations of the order parameter, which diverge through a phase transition[35–40].

Only below a second transition temperature $T^* = 97$ K does the quasi-elastic scattering intensity decrease, giving rise to a massive excitation, marked by the pale red shaded area in Fig. 1d for a few selected temperatures. The peak position determined from the fit is shown with pale red squares in Fig. 1c. Interestingly, neither bulk magnetization, nor specific heat shows any hint of this phase transition T^* (see Supplementary Fig. 1 and Supplementary Note 1). Despite these missing fingerprints, the dispersion of the A peak suggests that this mode may be linked to some bond spin-nematic order parameter η, which lowers the crystalline symmetry of the pyrochlore lattice below T^*.

The full temperature evolution of the A-mode is given in the panels of Fig. 1e–g, where we analyze frequency, line width, and intensity of this excitation. Figure 1g additionally plots the intensity over temperature of the quasi-elastic signal for direct comparison. Comparing the thermal evolution of the A-mode (red squares) with that of the 25 meV one-magnon mode (green diamonds), we notice a fundamentally different behavior. The nearly temperature-independent energy of the one-magnon excitation stands in stark contrast to the dramatic softening of mode A, which instead follows an order-parameter-like behavior that can be described by a critical exponent, i.e., $\omega(T) = a |T - T^*|^\beta$, with a being a scaling factor, $T^* = (97 \pm 5)$ K the critical temperature, and $\beta = 0.4 \pm 0.1$ the critical exponent. Likewise, while the linewidth of the one-magnon mode at 25 meV remains close to constant over a wide temperature range and up to T_N, the width of the A-mode broadens significantly with increasing temperature. Finally, the intensity of the 25-meV mode gradually drops off and approaches 0 around T_N, indicating a decreasing magnetic moment of the Ru ions upon approaching T_N. The A-mode, instead, evidences a quick drop in intensity with increasing temperature and disappears at T^*. As detailed in Supplementary Note 7 and Supplementary Fig. 7, the thermal evolution of the 32 meV excitation mirrors that of the 25-meV one.

Considering all of the above, we can confidently rule out a one-magnon scattering process to be related to the A-mode. Likewise, a purely phononic origin of this mode might be ruled out, since preliminary neutron scattering data on powder samples show no hint of a phonon mode at 3 meV at 1.5 K, although ultimately neutron data at higher wave vector and higher temperature might be needed [S. Choi, private communication]. We also emphasize that neither optical phonons, nor zone-folded acoustic phonons would be expected at such low energies in pyrochlore systems with this or similar elemental composition[41]. Zone-folding effects can be further discarded by taking the dominating spectral weight of the A-mode into account, which would require a significant

degree of lattice anharmonicity. No other structural refinement method however has lead to the observation of such dramatic structural effects. In addition, the rather sharp linewidth of the mode at base temperature underlines the coherent nature of the corresponding excitations, which agrees with the picture of fluctuation of some magnetic order parameter.

Lattice dynamics and its connection to the bond nematic amplitude mode

Evidence for the A-mode arising through fluctuations of a nematic order parameter can be also found in the lattice dynamics. To uncover such spin-related phonon anomalies, we now investigate the enhanced lattice dynamics in $Nd_2Ru_2O_7$ which we observe down to about half of T_N. As the E_g phonon involves twisting motions of the RuO_6 octahedra, it is rather susceptible to the changes in the Ru-O-Ru bond angle. Therefore, it justifies a strong spin-elastic coupling between the E_g phonon and Ru magnetic moments, and such coupling serves as a sensitive local probe to the onset of magnetic order or even to an enhancement of spin-spin correlations within Ru tetrahedra. In Fig. 2a we present the mid-energy range of the E_g symmetry channel, which is dominated by the E_g phonon at 40 meV. The arrows at 35 and 52 meV mark small leakage of phonons from the T_{2g} channel. Below T_N a giant softening of the phonon frequency is observed, followed by a highly dynamical, fluctuating regime in which the phonon splits into a dominating low-energy mode (~ 38 meV) and a weaker high-energy shoulder (~ 41 meV). Below T^*, the lattice dynamics resumes its rather static behavior.

Figure 2b highlights the lineshape of the E_g phonon, which is highly asymmetric and can be described by a Fano lineshape at room temperature. The 5 K spectrum evidences a nearly symmetric Lorentzian phonon lineshape. The appearance of an asymmetric Fano lineshape is generally ascribed to the inter-ference of a discrete (phonon) mode with an underlying, broad continuum of excitations[42]. A similar temperature dependence has been observed in the all-in-all-out pyrochlore compound $Cd_2Os_2O_7$[43], where it was related to a metal-insulator transition driven by spin-charge-lattice coupling. We recall that $Nd_2Ru_2O_7$ remains electrically insulating across the investigated temperature regime[29], therefore we rule out an electronic continuum as the origin (for details on the electronic band structure, see[44]). Instead, incoherent spin fluctuations of the paramagnetic phase ($T > T_N$) are a natural candidate for the broad continuum, as reported in the pyrochlore iridate $Eu_2Ir_2O_7$[34]. Upon passing through T_N, the spectral weight of the continuum is transferred towards quasi-elastic scattering and eventually to the low-energy A-mode. Thus, below T^* the interference between the broad magnetic continuum and the E_g phonon mode disappears and the phonon approaches a symmetric Lorentzian lineshape at low temperatures.

An analysis of the phonon peak parameters frequency, linewidth, intensity, and Fano asymmetry is presented in Fig. 2c–f. Both frequency and linewidth can be described by anharmonic behavior for $T > T_N$ (see solid red line and Supple-mentary Note 8 for details)[45]. Below T_N, this anharmonic behavior is abruptly halted and replaced by an enormous energy softening, peak broadening, and line splitting. A softening of the E_g phonon with the onset of magnetic order is commonly observed in pyrochlore magnets[46–48]. The giant softening from 41 meV down to 38 meV, present in $Nd_2Ru_2O_7$, however, exceeds these common values by about one order of magnitude. The dramatically enhanced linewidth in between the transition temperatures signals the opening of an effective decay channel in the form of additional spin fluctuations. Simultaneously, the intensity of the dominating line starts to increase monotonically, and the Fano asymmetry drops and approaches zero towards lowest tempera-tures. All these phonon anomalies underline the existence of a highly dynamical lattice that strongly couples to spin degrees of
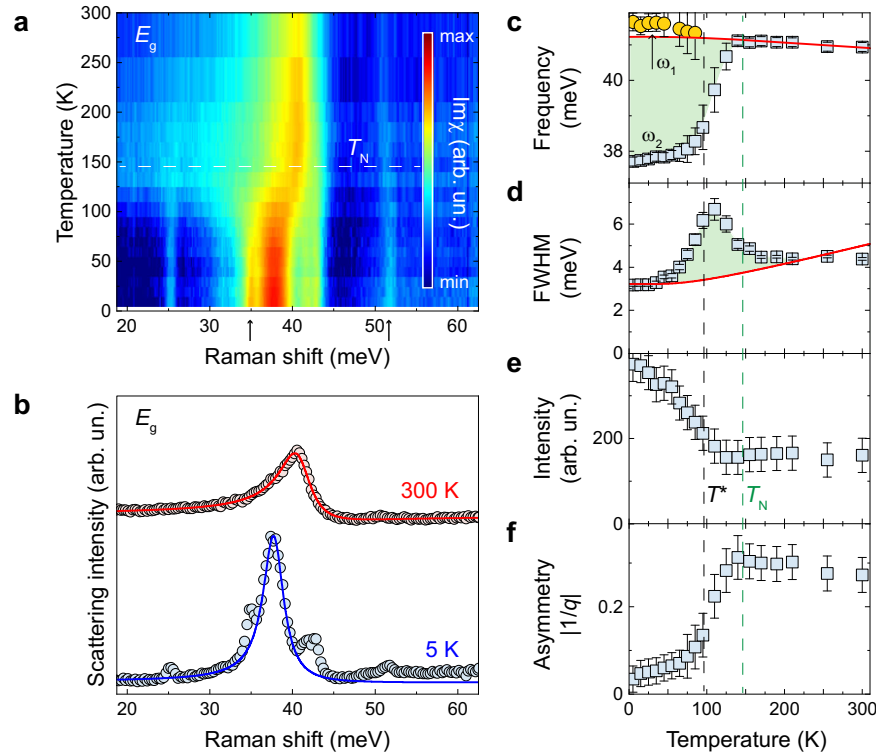
Fig. 2 Giant spin-phonon coupling in $Nd_2Ru_2O_7$. a Color contour plot of the mid-energy range focusing on the thermal evolution of the E_g channel. Arrows mark leakage of phonons from the T_{2g} channel. **b** Phonon spectra of the E_g channel measured at 5 K and at 300 K (symbols) together with asymmetric Fano fits to the dominating E_g phonon mode (solid lines). **c-f** Temperature-dependence of the phonon parameters frequency, linewidth (FWHM), peak intensity, and Fano asymmetry for the E_g phonon. The solid red lines are fits to the frequency and linewidth, corresponding to anharmonic softening and broadening, respectively (see text for details). Deviations from this anharmonic behavior are shaded in pale-green. T_N and T^* are marked by dashed lines. Error bars in (**c-f**) indicate ± 1 standard deviation around the mean value.

freedom, which settle in modulated or canted spin structures and culminate in the formation of an amplitude mode, i.e., the A-mode at 3 meV.

Broken symmetries

With the dynamic aspect of various Raman modes, we now turn to an analysis of the symmetry properties of various excitations in $Nd_2Ru_2O_7$. As we already detailed in Fig. 1a, b, the A-mode displays a striking two-fold symmetry in both parallel and crossed scattering configurations, which is at odds with the given cubic crystal structure. If the anomalous lattice dynamics of the E_g mode is indeed from coupling to magnetic bond-energy fluctuations, there should be some evidence of this coupling in its symmetry properties as well. Therefore, we now investigate the symmetries of the phonon modes.

Figure 3 a shows polar plots of phonon intensities of different symmetries, measured at $T = 5$ K in parallel (xx, red circles) and crossed (xy, black squares) polarization (see Supplementary Fig. 3 for the full data set). The experimental data for the A_{1g} and T_{2g} modes match their fits very well, which are denoted by solid lines based on the respective Raman tensors given in Supplementary Note 2. In contrast, the splitting of the E_g phonon mode into ω_1 and ω_2 lowers the symmetry of the resulting branches observed in parallel polarization from four-fold to two-fold rotationally symmetric (Fig. 3b), thus pointing towards a lowering symmetry of the RuO_6 octahedra. Without structural distortion, such lowering symmetry can be triggered from a spin bond order parameter $\langle \mathbf{f}_\eta \rangle = (\langle f_1 \rangle, \langle f_2 \rangle)$, where $f_1 = [(\mathbf{S}_1 + \mathbf{S}_2) \cdot (\mathbf{S}_3 + \mathbf{S}_4) - 2\mathbf{S}_1 \cdot \mathbf{S}_2 - 2\mathbf{S}_3 \cdot \mathbf{S}_4]/\sqrt{12}$ and $f_2 = (\mathbf{S}_1 - \mathbf{S}_2) \cdot (\mathbf{S}_3 - \mathbf{S}_4)/2$, as proposed in[49]. Such spin bond order parameter measures bond energy differences within the Ru tetrahedron, and couples directly

to the E_g phonon mode through the spin-elastic coupling $\mathbf{f}_\eta \cdot \mathbf{u}_{E_g}$. In crossed polarization, both branches still appear with the same four-fold symmetry (see Fig. 3b and Supplementary Fig. 3]. Both the splitting and the symmetry reduction are reminiscent of a nematic-like phase transition[50]. We can rule out any significant misalignment of the crystal or contributions from (potentially existing) neighboring domains as sources for these distorted polar plots, since all other phonons closely follow their expected rotational symmetry and only the E_g mode is affected.

In Fig. 3c we quantify the energy difference between ω_1 and ω_2 by introducing $\eta = (\omega_1 - \omega_2)/(\omega_1 + \omega_2)$, a phonon anisotropy parameter[51], which can be associated with the spin bond order parameter $\langle \mathbf{f}_\eta \rangle$, and we treat η as the nematic order parameter. Figure 3d sketches the ionic displacement patterns corresponding to the two-fold degenerate E_g phonon mode. Upon distortion of the local octahedral environment within a unit cell, this two-fold degeneracy may be lifted, resulting in a splitting of the E_g phonon. Previous studies on $Nd_2Ru_2O_7$ have not found any indication of a structural phase transition within our temperature range of interest, with experimental methods ranging from synchrotron and x-ray diffraction[29,52], to neutron diffraction[31]. However, a pronounced, non-monotonic decrease in the Ru-O-Ru angle was observed between 150 and 100 K[52]. This can indicate a gradual canting or rearrangement of spins in a (short-ranged) antiferromagnet or a transition among two neighboring phases with decreasing temperature, accompanied by strong bond-energy fluctuations and manifested by the observed entangled spin-lattice instabilities. This concept of competing bond configurations has also been explored, e.g., in breathing pyrochlores[53,54], while spin-lattice coupling in a 2D magnet lead to the splitting of an E_g phonon, albeit of smaller magnitude[55]. The temperature
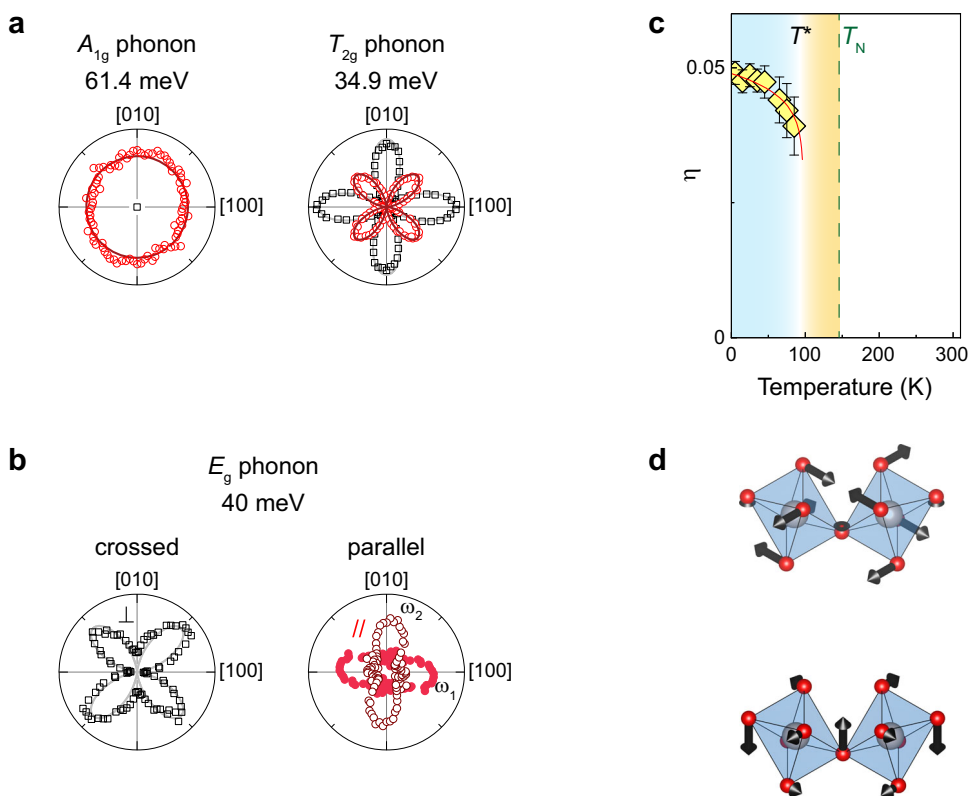
Fig. 3 Evidence for symmetry breaking in Nd$_2$Ru$_2$O$_7$. a Polarization plots for phonons of A_{1g}, T_{2g}, and **b** E_g symmetry measured in parallel (red circles) and in crossed (black squares) configuration at $T = 5$ K. The solid red and gray lines trace the theoretical rotational anisotropy following the respective Raman tensors. **c** The nematic order parameter $\eta(T)$ as extracted from the phonon frequencies shown in Fig. 2c. **d** Arrows sketch the ionic displacement patterns of the doubly degenerate E_g mode. Error bars in **c** indicate ± 1 standard deviation around the mean value.

dependence of η closely follows that of the A-mode, hence its emergence below 97 K indicates the onset of nematic order. Also, the fact that the two-fold, distorted E_g polar plot resembles the rotational symmetry of excitation A, as shown in Fig. 1a and b, suggests a direct correlation between the amplitude A-mode and lattice degrees of freedom of the RuO$_6$ octahedra.

DISCUSSION

With the broken symmetry identified, we wish to discuss the origin of the A-mode. In the related antiferromagnet Ca$_2$RuO$_4$[3,56] a broader Higgs mode at high energies (centered around 40 meV) is reported to stabilize through a condensation of $J = 1$ excitons per Ru site[28]. This single-ion picture may however not be relevant for the stabilization of the A-mode in Nd$_2$Ru$_2$O$_7$, given its smaller energy scale and the fact that it emerges through a second phase transition within the magnetically-ordered phase. Instead, narrow spectral features at low energies with dominating scattering intensity—strikingly similar to the A-mode—have been observed via Raman spectroscopy and interpreted as Higgs-type amplitude modes in the charge-density-wave compounds GdTe$_3$[5], 2H-TaS$_2$[57], and NbSe$_2$[58].

Based on these considerations and on the observed lattice dynamics, we can pinpoint the following scenario for the formation of the A-mode: At T_N, when the order of the Ru magnetic moments develops and translational symmetry breaks, the spin bond order parameter $\langle \mathbf{f}_\eta \rangle$ remains zero, since the magnetic energy of the six bonds in a single tetrahedron is uniform. However, through the spin-elastic coupling to the E_g phonon, the magnetic energy of the system can be further lowered. This drives the development of the spin-nematic bond

order, an example of vestigial order which grows out of the magnetic fluctuations, and in the temperature range between 97 K and 147 K leads to strong quasi-elastic scattering (Fig. 1d). Below 97 K, the energy of the A-mode grows as an order parameter (Fig. 1c). This order breaks the discrete rotational symmetry since it leads to inequality between bond energies on the Ru tetrahedron but preserves the translational symmetry, i.e., it is a $\mathbf{q} = 0$ order. The consequences of the spin nematic order also have a feedback to the lattice, causing the splitting of the E_g phonon with reduced two-fold symmetry through the spin-elastic coupling $\mathbf{f}_\eta \cdot \mathbf{u}_{E_g}$. Within this picture, T^* is the spin-nematic transition further lowering the symmetry of the system.

Remarkably, a two-fold symmetric amplitude Higgs mode was recently reported in the charge-density-wave ordered GdTe$_3$ in Raman scattering experiments of both parallel and crossed polarization configurations[5]. As such low symmetry is also inconsistent with the scalar nature of the Higgs mode, a polarization-dependent mechanism of constructive/destructive pathway interference was invoked, which instead yields an exotic axial Higgs mode. The striking similarities between GdTe$_3$ and Nd$_2$Ru$_2$O$_7$ raise the exciting prospect of stabilizing an axial Higgs mode of magnetic nature in pyrochlore systems with multiple spontaneously broken symmetries, e.g., both magnetic and nematic order. A deeper insight into the spin dynamics and requires a temperature-dependent study of the magnon band structure, e.g., via inelastic neutron scattering or resonant elastic x-ray scattering experiments. In addition, second-harmonic generation studies may shine further light on the nature of broken symmetries. However, these methods require sizable single crystals with flat or cleavable surfaces. Given the availability of suitable single crystals, such future studies will be essential to

unambiguously uncover the nature of the observed amplitude mode in $Nd_2Ru_2O_7$.

In summary, we uncover a wide temperature regime of coupled spin and lattice fluctuations in the pyrochlore ruthenate $Nd_2Ru_2O_7$ via Raman spectroscopy that result in a second phase transition T^*, which has been elusive in other thermodynamic probes. A low-energy excitation emerging out of these fluctuations with a distinct symmetry and a peculiar temperature evolution is interpreted as a coherent amplitude mode out of nematic order. Future studies under extreme conditions, such as high pressure and magnetic fields, are envisaged to tune these fluctuations and further pinpoint the nature of the low-energy Higgs mode.

METHODS

Sample growth

Single crystals of $Nd_2Ru_2O_7$ were synthesized using the KF flux method[59]. Typical resulting crystals of about $30 \times 30 \times 30\ \mu m^3$ volume exhibit shiny triangular- and rectangular-shaped as-grown surfaces, corresponding to [111] and [100] facets, respectively. Based on our obtained Raman spectra and basic thermodynamic characterization [see Supplementary Note 1] we can rule out any inclusion of a secondary Nd_3RuO_7 phase, commonly found in pyrochlore ruthenates[29,60].

Raman scattering

Raman spectroscopic experiments have been carried out using a $\lambda = 532$ nm solid state laser (Cobolt Samba) with a spot diameter of about $10\ \mu m$ and an incident laser power at the sample position below 0.35 mW to reduce local laser heating effects. The scattered light passed through a volume Bragg grating notch filter set (Optigrate) to discriminate the laser line and to access Raman signals with energies as low as 0.8 meV. The sample was mounted via silver epoxy onto the cold finger of a He-cooled open-flow cryostat (Oxford Microstat HiRes). The Raman-scattered light was dispersed through a single-stage Horiba iHR 320 spectrometer with a 1800 gr/mm grating onto a Horiba Synapse CCD. In this configuration, a spectral resolution of about $1.2\ cm^{-1}$/pixel is achieved. A constant background (dark current) of 117 counts was subtracted from each spectrum. Where indicated, Bose-corrected Raman intensity $Im\chi(\omega)$ is plotted. It is related to the as-measured Raman intensity $I(\omega)$ via the fluctuation-dissipation theorem by $I(\omega) = [1 + n(\omega)]Im\chi$, where $n(\omega)$ is the Bose factor.

DATA AVAILABILITY

All data needed to evaluate the conclusions in the paper are present in the paper and/or the Supplementary Materials. All data are available from the corresponding authors upon request.

REFERENCES

1. Higgs, P. W. Broken symmetries and the masses of gauge bosons. *Phys. Rev. Lett.* **13**, 508–509 (1964).
2. Shimano, R. & Tsuji, N. Higgs mode in superconductors. *Annu. Rev. Cond. Mat. Phys.* **11**, 103–124 (2020).
3. Jain, A. et al. Higgs mode and its decay in a two-dimensional antiferromagnet. *Nat. Phys.* **13**, 633–637 (2017).
4. Rüegg, C. H. et al. Quantum magnets under pressure: controlling elementary excitations in $TlCuCl_3$. *Phys. Rev. Lett.* **100**, 205701 (2008).
5. Wang, Y. et al. Axial Higgs mode detected by quantum pathway interference in RTe_3. *Nature* **606**, 896–901 (2022).
6. Marsh, D. J. E. Axion cosmology. *Phys. Rep.* **643**, 1–79 (2016).
7. Franzosi, D. B., Cacciapaglia, G., Cai, H., Deandrea, A. & Frandsen, M. Vector and axial-vector resonances in composite models of the Higgs boson. *J. High. Energy Phys.* **2016**, 76 (2016).
8. Cao, G. & DeLong, L. *Frontiers of 4d- and 5d-transition metal oxides*. (World Scientific Publishing Co. Pte. Ltd., Singapore, 2013).
9. Takayama, T., Chaloupka, J., Smerald, A., Khaliullin, G. & Takagi, H. Spin-orbit-entangled electronic phases in 4d and 5d transition-metal compounds. *J. Phys. Soc. Jpn* **90**, 062001 (2021).
10. Kitaev, A. Anyons in an exactly solved model and beyond. *Ann. Phys.* **321**, 2–111 (2006).
11. Jackeli, G. & Khaliullin, G. Mott insulators in the strong spin-orbit coupling limit: From Heisenberg to a quantum compass and Kitaev models. *Phys. Rev. Lett.* **102**, 017205 (2009).
12. Takagi, H., Takayama, T., Jackeli, G., Khaliullin, G. & Nagler, S. E. Concept and realization of Kitaev quantum spin liquids. *Nat. Rev. Phys.* **1**, 264–280 (2019).
13. Trebst, S. & Hickey, C. Kitaev materials. *Phys. Rep.* **950**, 1–37 (2022).
14. Mackenzie, A. P., Scaffidi, T., Hicks, C. W. & Maeno, Y. Even odder after twenty-three years: the superconducting order parameter puzzle of Sr_2RuO_4. *npj Quantum Mater.* **2**, 40 (2017).
15. Bramwell, S. T. & Gingras, M. J. P. Spin ice state in frustrated magnetic pyrochlore materials. *Science* **294**, 1495–1501 (2001).
16. Gingras, M. J. P. & McClarty, P. A. Quantum spin ice: a search for gapless spin liquids in pyrochlore magnets. *Rep. Prog. Phys.* **77**, 056501 (2014).
17. Lefrançois, E. et al. Fragmentation in spin ice from magnetic charge injection. *Nat. Commun.* **8**, 209 (2017).
18. Pace, S. D., Morampudi, S. C., Moessner, R. & Laumann, C. R. Emergent fine structure constant of quantum spin ice is large. *Phys. Rev. Lett.* **127**, 117205 (2021).
19. Li, F.-Y. et al. Weyl magnons in breathing pyrochlore antiferromagnets. *Nat. Commun.* **7**, 12691 (2016).
20. Wang, K. et al. Unconventional free charge in the correlated semimetal $Nd_2Ir_2O_7$. *Nat. Phys.* **16**, 1194–1198 (2020).
21. Hwang, K., Trivedi, N. & Randeria, M. Topological magnons with nodal-line and triple-point degeneracies: Implications for thermal Hall effect in pyrochlore iridates. *Phys. Rev. Lett.* **125**, 047203 (2020).
22. Gao, Y.-H., Yao, X.-P., Li, F.-Y. & Chen, G. Spin-1 pyrochlore antiferromagnets: Theory, model, and materials' survey. *Front. Phys.* **15**, 63201 (2020).
23. Gardner, J. S., Gingras, M. J. P. & Greedan, J. E. Magnetic pyrochlore oxides. *Rev. Mod. Phys.* **82**, 53–107 (2010).
24. Haldane, F. D. M. Nonlinear field theory of large-spin Heisenberg antiferromagnets: Semiclassically quantized solitons of the one-dimensional easy-axis Néel state. *Phys. Rev. Lett.* **50**, 1153–1156 (1983).
25. Wang, C., Nahum, A. & Senthil, T. Topological paramagnetism in frustrated spin-1 Mott insulators. *Phys. Rev. B* **91**, 195131 (2015).
26. Li, F.-Y. & Chen, G. Competing phases and topological excitations of spin-1 pyrochlore antiferromagnets. *Phys. Rev. B* **98**, 045109 (2018).
27. Buessen, F. L., Hering, M., Reuther, J. & Trebst, S. Quantum spin liquids in frustrated spin-1 diamond antiferromagnets. *Phys. Rev. Lett.* **120**, 057201 (2018).
28. Khaliullin, G. Excitonic magnetism in Van Vleck-type d⁴ Mott insulators. *Phys. Rev. Lett.* **111**, 197201 (2013).
29. Gaultois, M. W. et al. Structural disorder, magnetism, and electrical and thermoelectric properties of pyrochlore $Nd_2Ru_2O_7$. *J. Phys.: Condens. Matter* **25**, 186004 (2013).
30. Ito, M. et al. Neutron diffraction study of pyrochlore compound $R_2Ru_2O_7$ ($R=Y$, Nd) above and below the spin freezing temperature. *J. Phys. Soc. Jpn* **69**, 888–894 (2000).
31. Ku, S. T. et al. Low temperature magnetic properties of $Nd_2Ru_2O_7$. *J. Phys.: Condens. Matter* **30**, 155601 (2018).
32. Nguyen, T. H. et al. Topological magnon band crossing in $Y_2Ir_2O_7$. *Phys. Rev. Lett.* **127**, 267203 (2021).
33. Lee, J. H. et al. Linear scaling relationship of Neel temperature and dominant magnons in pyrochlore ruthenates. *Phys. Rev. B*, preprint at https://arxiv.org/abs/2304.08815 (2023).
34. Ueda, K. et al. Phonon anomalies in pyrochlore iridates studied by Raman spectroscopy. *Phys. Rev. B* **100**, 115157 (2019).
35. Gallais, Y. & Paul, I. Charge nematicity and electronic Raman scattering in iron-based superconductors. *C. R. Phys.* **17**, 113–139 (2016).
36. Lemmens, P., Güntherodt, G. & Gros, C. Magnetic light scattering in low-dimensional quantum spin systems. *Phys. Rep.* **375**, 1–103 (2003).
37. Wang, Y. et al. The range of non-Kitaev terms and fractional particles in α-$RuCl_3$. *npj Quantum Mater.* **5**, 14 (2020).
38. Reiter, G. F. Light scattering from energy fluctuations in magnetic insulators. *Phys. Rev. B* **13**, 169–173 (1976).
39. Lyons, K. B. & Fleury, P. A. Magnetic energy fluctuations: observations by light scattering. *Phys. Rev. Lett.* **48**, 202–205 (1982).

40. Kim, K. et al. Direct observation of excitonic instability in Ta_2NiSe_5. *Nat. Commun.* **12**, 1969 (2021).

41. Kim, T. et al. Spin-orbit coupling effects on spin-phonon coupling in $Cd_2Os_2O_7$. *Phys. Rev. B* **102**, 201101(R) (2020).

42. Fano, U. Effects of configuration interaction on intensities and phase shifts. *Phys. Rev.* **124**, 1866–1878 (1961).

43. Nguyen, T. M. H. et al. Two-magnon scattering in the 5d all-in-all-out pyrochlore magnet $Cd_2Os_2O_7$. *Nat. Commun.* **8**, 251 (2017).

44. https://legacy.materialsproject.org/materials/mp-19930/#electronic-structure.

45. Balkanski, M., Wallis, R. F. & Haro, E. Anharmonic effects in light scattering due to optical phonons in silicon. *Phys. Rev. B* **28**, 1928–1934 (1983).

46. Lee, J. S. et al. Strong spin-phonon coupling in the geometrically frustrated $Y_2Ru_2O_7$. *Phys. Rev. B* **69**, 214428 (2004).

47. Thomas, A. et al. Role of spin-phonon and electron-phonon interactions in the phonon renormalization of $(Eu_{1-x}Bi_x)_2Ir_2O_7$ across the metal-insulator phase transition: temperature-dependent Raman and x-ray studies. *Phys. Rev. B* **105**, 075145 (2022).

48. Son, J. et al. Unconventional spin-phonon coupling via the Dzyaloshinskii-Moriya interaction. *npj Quantum Mater.* **4**, 17 (2019).

49. Tchernyshyov, O., Moessner, R. & Sondhi, S. L. Spin-Peierls phases in pyrochlore antiferromagnets. *Phys. Rev. B* **66**, 064403 (2002).

50. Yao, Y. et al. An electronic nematic liquid in $BaNi_2As_2$. *Nat. Commun.* **13**, 4535 (2022).

51. Zhang, W.-L., Sefat, A. S., Ding, H., Richard, P. & Blumberg, G. Stress-induced nematicity in $EuFe_2As_2$ studied by Raman spectroscopy. *Phys. Rev. B* **94**, 014513 (2016).

52. Chen, S.-W. et al. Low temperature structural anomalies arising from competing exchange interactions in pyrochlore $Nd_2Ru_2O_7$ probed by XRD and EXAFS. *Phys. Chem. Chem. Phys.* **17**, 23667–23673 (2015).

53. Lee, S. et al. Dichotomy in temporal and thermal spin correlations observed in the breathing pyrochlore $LiGa_{1-x}In_xCr_4O_8$. *npj Quantum Mater.* **6**, 47 (2021).

54. Dissanayake, S. et al. Towards understanding the magnetic properties of the breathing pyrochlore compound $Ba_3Yb_2Zn_5O_{11}$ through single-crystal studies. *npj Quantum Mater.* **7**, 77 (2022).

55. Tian, Y., Gray, M. J., Ji, H., Cava, R. J. & Burch, K. S. Magneto-elastic coupling in a potential ferromagnetic 2D atomic crystal. *2D Mater.* **3**, 025035 (2016).

56. Souliou, S.-M. et al. Raman scattering from Higgs mode oscillations in the two-dimensional antiferromagnet Ca_2RuO_4. *Phys. Rev. Lett.* **119**, 067201 (2017).

57. Grasset, R. et al. Pressure-induced collapse of the charge density wave and Higgs mode visibility in $2H-TaS_2$. *Phys. Rev. Lett.* **122**, 127001 (2019).

58. Measson, M.-A. et al. Amplitude Higgs mode in the $2H-NbSe_2$ superconductor. *Phys. Rev. B* **89**, 060503(R) (2014).

59. Millican, J. N. et al. Crystal growth and structure of $R_2Ir_2O_7$ (R = Pr, Eu) using molten KF. *Mater. Res. Bull.* **42**, 928–934 (2007).

60. Taira, N., Wakeshima, M. & Hinatsu, Y. Magnetic properties of ruthenium pyrochlores $R_2Ru_2O_7$. *J. Phys.: Condens. Matter* **11**, 6983–6990 (1999).

AUTHOR CONTRIBUTIONS

M.K.K., J.H.L., and D.S. synthesized high quality $Nd_2Ru_2O_7$ single crystals. J.K and D.W. performed Raman scattering experiments with the help of D.O., M.N., and H.C. D.W., J.K., and S.C. analyzed the data. L.E.C. and Y.B.K. calculated magnon band energies. H.-S.K. performed exact diagonalization calculations. Detailed symmetry considerations based on the Loudon-Fleury approach have been carried out by Y.Y. and N.B.P. D.W., Y.Y., N.B.P., C.K., and S.R.P. wrote the manuscript. All authors discussed the results and commented on the manuscript. D.W. and J.K. contributed equally to this work.

COMPETING INTERESTS

The authors declare no competing interests.

ADDITIONAL INFORMATION

Supplementary information The online version contains supplementary material available at https://doi.org/10.1038/s41535-023-00572-9.

Correspondence and requests for materials should be addressed to Changyoung Kim or Seung Ryong Park.

Reprints and permission information is available at http://www.nature.com/reprints

Publisher's note Springer Nature remains neutral with regard to jurisdictional claims in published maps and institutional affiliations.